PHOTONICS Research

Broadband omnidirectional visible spectral metamaterials

Jing Zhao,[1,3,†] Xianfeng Wu,[2,†] Di Cao,[2,†] Mingchao Zhou,[2] Zhijie Shen,[2] and Xiaopeng Zhao[2,*]

[1]Medtronic plc, Boulder, Colorado 80301, USA
[2]Smart Materials Laboratory, Department of Applied Physics, Northwestern Polytechnical University, Xi'an 710129, China
[3]e-mail: zhaojing1120@gmail.com
[†]These authors contributed equally to this work.
*Corresponding author: xpzhao@nwpu.edu.cn

Received 1 December 2022; revised 7 May 2023; accepted 7 May 2023; posted 9 May 2023 (Doc. ID 482542); published 23 June 2023

Optical metamaterials offer the possibility of controlling the behavior of photons similarly to what has been done about electrons in semiconductors. However, most optical metamaterials are narrowband, and they achieve negative refraction within a small window of incident angles, making them impractical for common visible light systems that operate effectively over a wide range of frequencies and directions. Considerable resistive loss at the resonant frequency of these metamaterials further prevents them from being deployed in the real world. Here, we develop a novel metamaterial randomly assembled by a list of narrowband, omnidirectional, and ultra-low-loss meta-cluster systems using a bottom-up approach. Weak interactions among numerous meta-cluster sets greatly broaden the effective bandwidth of the overall structure, exhibiting frequency selectivity and spatial modulation when responding to white-light illumination. We observe negative refraction in the 490–730 nm band, and observe an inverse Doppler effect at green, yellow, and red frequencies, across most of the visible spectrum. Our method allows for low-cost fabrication of sizable broadband omnidirectional three-dimensional metamaterial samples, which opens the door to the rapid development of optical metamaterials, micro–nano assembly and preparation, tunable optical device engineering, etc.

https://doi.org/10.1364/PRJ.482542

1. INTRODUCTION

Optical metamaterials provide a technical approach to constructing material spatial structures at the subwavelength scale to explore new optical phenomena [1,2]. The inverse Doppler effect provides a new type of radar for tunable and multi-frequency radiation source design [3], and broadband inverse Doppler effect provides a new technique for the study of cosmic effects such as celestial photonics [4] and exoplanet detection [5]. The optical transformation of metamaterials provides a new way of stealth [1], such as the three-dimensional (3D) invisibility cloak [6] and the ultrathin invisibility skin cloak for visible light at 730-nm wavelength [7]. However, metamaterial units can only show behavior at very narrow wavebands and in selected incident light directions, such as the metallic wires [8] and split-rings [9] building blocks for achieving negative refraction identified by Pendry in his pioneering works, and the double-fishnet structure for optical metamaterials [10,11]. The control of light from a wider band and different directions is a common need for various applications [12–14]. In the past, the increase of bandwidth usually comes at the cost of the increase of device volume, which is difficult to integrate into today's nanophotonic systems. Metamaterials have broad application prospects due to their compact size and high integration. However, the resonance and high dispersion characteristics of metamaterials' internal structure limit the working bandwidth, resulting in high absorption loss [15]. This raises questions about its practical usefulness, with broadband and omnidirectional issues being an important hurdle to overcome [12–14].

Numerical simulation shows that the symmetrical GHz 3D isotropic structure [16] and THz dual-anisotropic structure [17] have certain broadband properties. In the infrared band [18], the concavity of particles can make the resonance frequency tunable with the near-infrared spectrum broadband (1–2 μm). Using transform optics to design metamaterials [19], it is theoretically possible to achieve visible broadband metamaterials. The design of metamaterials based on the non-resonant [20,21] method avoids the resonance loss and bandwidth limitations, but often introduces new limitations such as polarization state. The local resonance internal temperament of optical metamaterials with high loss, narrow frequency, and orientation has become the bottleneck of the development of science. Recently, topological photonics has provided a new platform for manipulating the propagation of surface waves, such as negative refraction [22,23]. Although this method shows advantages in nonreflection and full-angle due to the

topological protection [23], the extension of topological photonics to optical frequency is rarely studied, and it is still highly challenging to realize omnidirectional negative refraction operating in the broadband visible spectrum.

The required structural features for optical negative-index metamaterials such as a metallic nanogap and complicated 3D networks would be difficult to achieve with conventional monolithic lithography [24]. Self-assembled colloidal soft materials have emerged as a new platform for the preparation of optical metamaterials, which can promote the massive and large-scale applications of optical metamaterials and accelerate the development of tunable optical devices with unprecedented functionality and performance characteristics [25]. Unfortunately, although an unnaturally high refractive index has been experimentally verified [24], these works were unable to reach the negative refractive index. Although plasmonic materials with a lower loss than noble metals have long been sought, stable sodium-based plasmonic devices with state-of-the-art performance at near-infrared wavelengths were not available until quite recently [26]. By engineering of the dispersion properties of a photonic crystal (PhC), the photonic bands for 3D PhCs capable of negative refraction in the mid-infrared were described [27]. Related developments have demonstrated that micro- and nano-structures of engineered disorder, a state between perfect order and complete randomness, could yield various new phenomena in the field of optics [28–30]. The concept of engineered disorder has disclosed possibilities of metamaterials with previously unimagined freedom of design [28]. The bottom-up [31–33] synthesis, a scalable and low-cost fabrication method, provides unparalleled control over the morphology and optical response of individual plasmonic building blocks [34]. Recently, our group proposed an optical metamaterial with an ultralow-loss isotropic ball-thorn-shaped meta-cluster structure, which makes it possible to assemble optical metamaterials from the bottom up [31]. However, broadband and omnidirectional issues are still unsolved.

Here, we propose a broadband omnidirectional ultralow-loss meta-cluster system in the visible band, and find that the cluster disordered assembly system has the phenomenon of automatic frequency selection response and spatial regulation change for abnormal behavior in the external field. Based on the weak interaction basis of local resonance elements [35–37], each ultralow-loss isotropic cluster in the system resonates at the natural frequency, and the total response of the system is the combination of each different type of single resonance spectrum. Theory and experiment prove that the cluster system shows weak interaction. Based on Mie scattering theory, the negative refractive index wavelength of visible light is 450–750 nm, and the cluster has omnidirectional response. Cluster elements of different geometric sizes were prepared by the bottom-up method. The planar films and wedge-shaped samples assembled automatically without selection showed weak interaction and omnidirectivity. The negative refractive index in the 490–730 nm band was observed by using the prepared 3D bulk sample; the lowest value of figure of merit (FOM) was 6.7 at 538 nm, and the highest value was 13 at 592 nm. A broadband inverse Doppler effect was observed. The anomalous behavior of the cluster disordered assembly system has the characteristics of automatic frequency selection response and spatial regulation, which reflects the completely different characteristics between a local resonance weak interaction system and a strong interaction system such as the PhC. The weak interaction of clusters breaks through the physical limitations of the design of broadband omnidirectional optical metamaterials, and the automatic frequency selection response and spatial position periodic modulation characteristics open the bottleneck of the bottom-up fabrication of 3D large-area materials, providing a common path for the rapid development of broadband omnidirectional optical metamaterials.

2. RESULT AND DISCUSSION

A. Broadband Omnidirectional Metamaterials Composed of Meta-Cluster System

As we all know, visible light is a kind of polychromatic light, which vibrates with the same intensity in all directions. A prism can decompose it into seven bands of light, each of which has a different color and frequency. Inspired by polychromatic light, utilizing an ultralow-loss isotropic ball-thorn-shaped meta-cluster [31], we propose a meta-cluster system showing broadband omnidirectional negative refraction in response to external field [Fig. 1(a)], which is in accord with the weak interaction characteristics of the metamaterial unit structure [35–37]. A cluster unit is composed of 12 meta-cluster [Fig. 1(b)] structures with different frequency bands [Fig. 1(c)]. Any meta-cluster works in the corresponding visible light frequency band, and the clusters can work together to realize the response in the visible light broadband. The single meta-cluster structure is composed of spherical nuclei and thin rods. In the simulation, the thin rod is first rotated at an equal angle around the z axis and then around the y axis to make sure the thin rods grow evenly on the surface of the spherical nuclei. The diameter of the rods is set as $d = 15$ nm, and the number of the rods is 600 in the simulation method, which is not exactly equivalent to the actual manufactured particles. The inner part of the bulb nucleus and the thin rod is titanium dioxide medium, and the skin is 1 nm thick silver. l represents the diameter of the entire meta-cluster structure, r represents the radius of the spherical core, W represents the lattice constant of the structural unit, and the surrounding medium is PMMA. The meta-cluster structure satisfies the Mie scattering principle, and transmission and reflection parameters can be obtained by numerical simulation (CST). Adjusting l, r, and W according to scaling rule enables the model to be applicable to different working frequency bands. The blue-light, green-light, yellow-light, and red-light meta-cluster models are designed as special showcase [Figs. 2(a)–2(l)]. As expected, the simulated transmission coefficient and reflection coefficient curves [Figs. 2(e)–2(h)] indicate that the meta-cluster structure resonates within the wavelength range of blue-light, green-light, yellow-light, and red-light, respectively. Correspondingly, derived from the Mie theory, the effective permeability, permittivity, and refractive index of the meta-cluster structure are simultaneously negative at near 490 nm [Fig. 2(i)], 530 nm [Fig. 2(j)], 590 nm [Fig. 2(k)], and 640 nm [Fig. 2(l)].

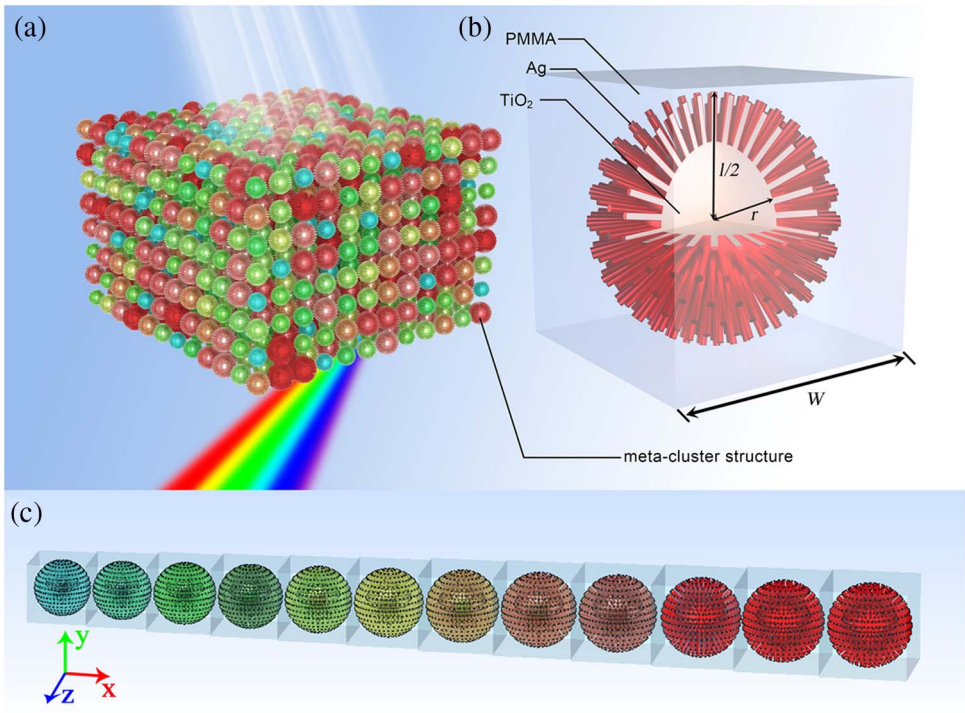

Fig. 1. Schematic and behavior of broadband omnidirectional meta-clusters system. (a) Negative refraction response of cluster system. (b) Structure of single cluster. (c) Cluster unit of broadband omnidirectional meta-clusters system (12 × 1 × 1); through the response bands of 480 nm, 500 nm, 530 nm, 550 nm, 570 nm, 590 nm, 620 nm, 640 nm, 660 nm, 680 nm, 700 nm, and 720 nm, the 12 cluster combinations basically cover the visible range and realize the response of visible light in broadband.

Regarding the origin of the Mie resonance, the distribution of the E-field, etc., of narrowband meta-clusters within their resonance wavelengths has been analyzed in the supplementary material of the Ref. [31]. The green- and red-light models individually respond specifically to the corresponding incident light and produce a negative refraction effect. In fact, each ball-thorn-shaped meta-cluster can be regarded as composed of 1200 meta-atoms: U-shaped split-ring and equivalent wires distributed evenly and symmetrically along the space [Fig. 1(b)]. The protruding rods and epidermic connections form "U" shaped effective units, and negative permeability is generated when the annular current and the external magnetic field interact with each other, resulting in Mie resonance. For the broadband model, it can be seen from Figs. 2(e)–2(l) that their transmission and reflection peaks appear only at the location of that particular meta-cluster, and the peak positions of the negative permittivity, negative permeability, and negative refractive index are consistent with that. To reveal the operating modes in the broadband model, we calculated a combined model consisting of two different green-light meta-clusters, and a combined model consisting of two different red-light meta-clusters (the parameters of the two green-light models are $l = 530$ nm, $r = 165$ nm, $W = 560$ nm and $l = 550$ nm, $r = 184$ nm, $W = 580$ nm, respectively; the parameters of the two red-light models are $l = 640$ nm, $r = 215$ nm, $W = 670$ nm and $l = 660$ nm, $r = 221$ nm, $W = 690$ nm, respectively). Figures 2(m) and 2(n) show the simulated results of the combined model composed of two green-light meta-clusters and two red-light meta-clusters, respectively, which indicate that the transmission and reflection peaks of the combined model appear only at specific frequency positions. It can be concluded from the resonance positions in Figs. 2(m) and 2(n) that only specific meta-clusters in the broadband model are active at the corresponding frequencies. These results are consistent with the weak interaction principle found in Ref. [37]. Accordingly, a series of meta-clusters with frequency spacing were designed to obtain broadband samples and achieve broadband negative refractive index.

Figure 2(o) shows the broadband refractive index curve (black curve) of visible light obtained based on parameter extraction of a 12 × 1 × 1 clusters unit [Fig. 1(c)]. The negative refractive index fluctuates between −0.5 and −0.4, and the response frequency band of negative refractive index reaches 450–750 nm, which almost covers the whole frequency band of visible light. The green and red dotted lines in the figure are the calculation results of single-frequency green- and red-light models. The minimum negative refractive index reaches −0.47 at 538 nm and −0.45 at 645 nm, respectively. The corresponding quality factor FOM curve is shown in Fig. 2(p); $\mathrm{FOM_{sim}} = -\mathrm{Re}(n)/\mathrm{Im}(n)$, for $\mathrm{Re}(n) < 0$, $\mathrm{Re}(n)$ and $\mathrm{Im}(n)$ are the real and imaginary parts of the simulated complex refractive index, respectively, and FOM value shows a zigzag downward trend with the wavelength red shift. Significant FOM ranges (greater than 8) from 473 nm to 706 nm, with a maximum of 15.52 at 497 nm. Due to the weak interaction among clusters, the frequency of negative refraction is greatly widened compared with that of single frequency, and there is no restriction on the directivity of incident light, forming omnidirectional response.

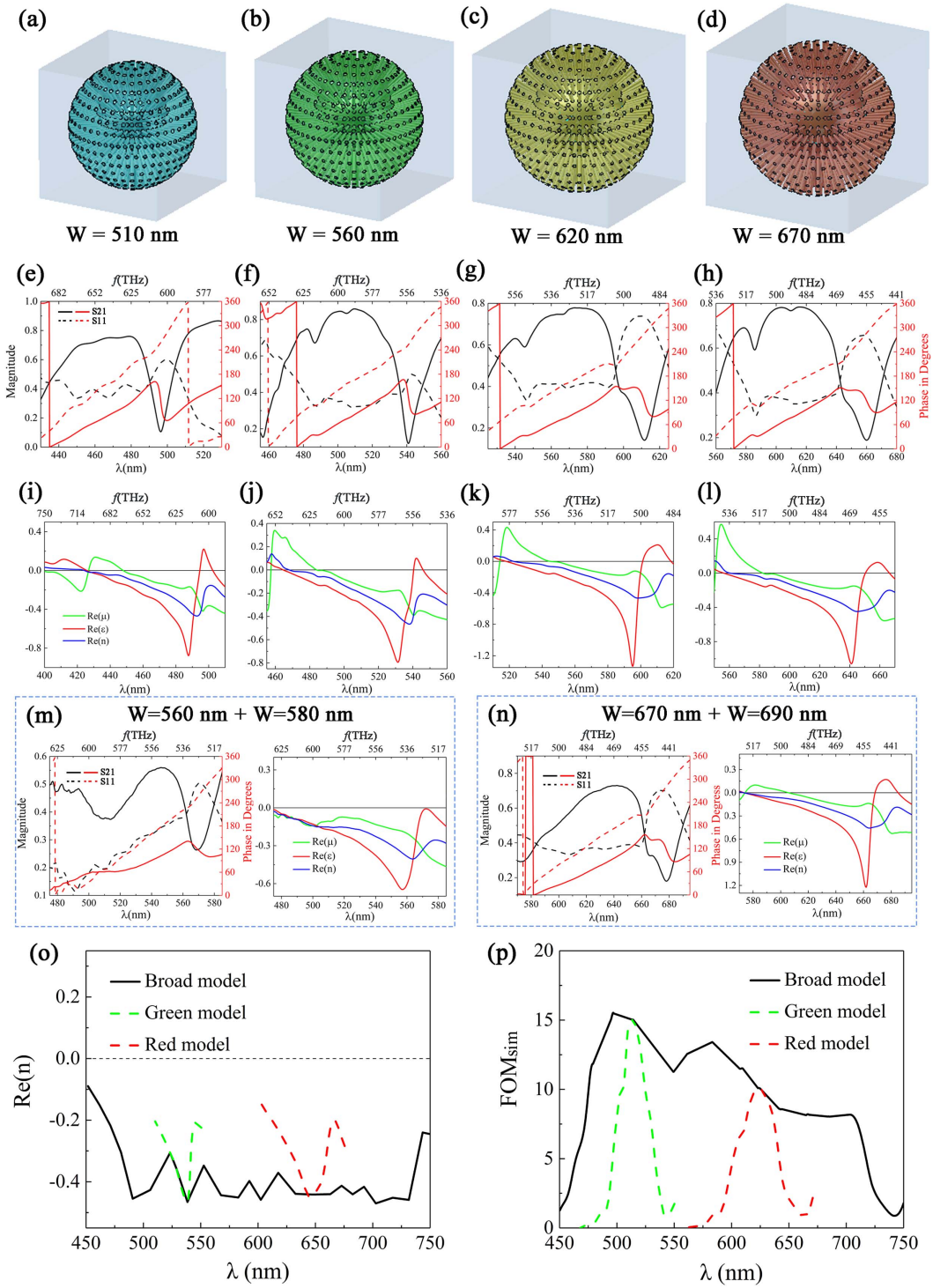

Fig. 2. Simulated behavior of meta-cluster structure. (a)–(d) Meta-cluster model in blue-light, green-light, yellow-light, and red-light wavebands, respectively. The cluster is composed of a spherical core and 600 prominent rods; both the kernel and rods are made of TiO_2 coated by Ag of 1 nm thickness. The diameter of the rod is 15 nm. l represents the diameter of the meta-cluster, r is the radius of the spherical kernel, and W refers to the lattice constant of the meta-cluster. Parameters are (a) $l = 480$ nm, $r = 146$ nm, and $W = 510$ nm; (b) $l = 530$ nm, $r = 165$ nm, and $W = 560$; (c) $l = 590$ nm, $r = 198$ nm, and $W = 620$ nm; and (d) $l = 640$ nm, $r = 215$ nm, and $W = 670$ nm. (e)–(h) Transmission (solid line) and reflection (dotted–dashed line) coefficient curves of the meta-clusters in (a)–(d), correspondingly. (i)–(l) Effective parameters (permeability, permittivity, and refractive index) retrieved from the coefficients in (e)–(h), respectively. (m) Simulated results of the model composed of two green-light meta-clusters with $l = 530$ nm, $r = 165$ nm, $W = 560$ nm and $l = 550$ nm, $r = 184$ nm, $W = 580$ nm. (n) Simulated results of the model composed of two red-light meta-clusters with $l = 640$ nm, $r = 215$ nm, $W = 670$ nm and $l = 660$ nm, $r = 221$ nm, $W = 690$ nm. (o) Negative refractive index curve in visible light broadband obtained by parameter inversion using Mie theory. (p) FOM curve of quality factor corresponding to (o). In (o) and (p), the green and red dotted lines are the simulated results of the single-frequency models [31] corresponding to the green and red bands, respectively.

In addition, the FOM value of the whole band range shows good low-loss performance.

It can be seen that our meta-cluster has the same size as the incident wavelength, which is somewhat similar to a PhC. However, the geometrical size of these meta-atoms (U-shaped split-ring and equivalent wires) is much smaller than the wavelength, and it is their independent resonance that forms the meta-cluster resonant response outfield. Different from the collective resonance of PhC with strong periodic structure, the metamaterials are weakly acting structures where the behavior of the system is revealed by each cluster or clusters independently. Therefore, the periodicity and arrangement of the system structure have little influence on the behavior, and the broadband omnidirectional abnormal behavior depends on the composition of the cluster.

B. Metamaterials Assembled by Meta-Cluster System

Eight kinds of Ag/AgCl/TiO_2@PMMA (meta-cluster) nanoparticles were prepared by solvothermal synthesis from bottom to top. The transmission electron microscopy (TEM) images of the meta-cluster particles that resonate in the red- [Fig. 3(a)], yellow- [Fig. 3(b)], and green- [Fig. 3(c)] light spectra reveal a classic kernel (AgCl/TiO_2)–shell (PMMA) structure. The images confirm the presence of PMMA filling between different nanorods, and the thickness of the PMMA shell is nearly 20–30 nm. According to the idea of multi-frequency composite (see Appendix B), the meta-cluster particle system in the wide band of visible light was prepared [Fig. 3(d)]. The meta-cluster particle set was assembled into a single dense broadband film

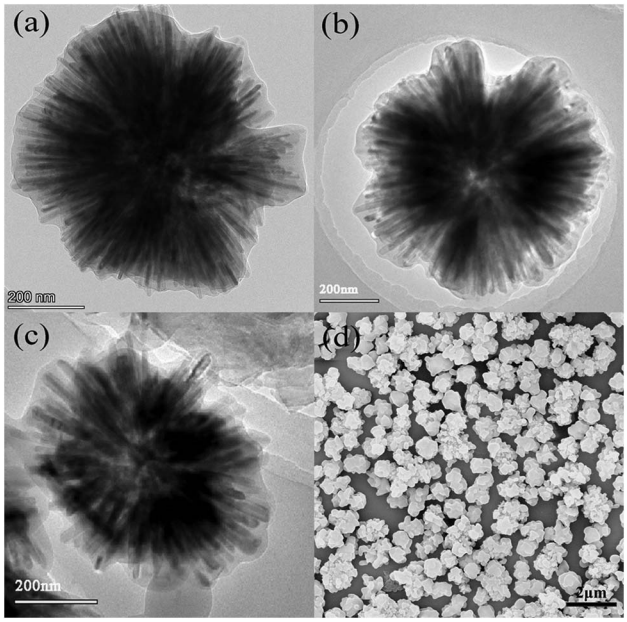

Fig. 3. Morphology and characterization of the Ag/AgCl/TiO_2@PMMA particles resonating in visible light broadband. TEM images of Ag/AgCl/TiO_2@PMMA particles: (a) red-light particle, (b) yellow-light particle, and (c) green-light particle. (d) SEM image of the monolayer film of the broadband metamaterial, which is obtained by mixing eight kinds of single-frequency Ag/AgCl/TiO_2@PMMA particles.

sample with a size of 10 mm × 18 mm and a thickness of ~0.7 μm by microflow injection [Figs. 4(a) and 4(b)]. A 3D wedge-shaped sample with an angle of ~1.4°, width of 5 mm, and length of 2 mm was prepared from self-assembled meta-cluster particles. Figures 4(c) and 4(d) show the optical micrograph and scanning electron microscopy (SEM) images of the micromorphology of the side portion of the wedge angle. The actual wedge angle is stacked with about 30 layers of particles at the highest point and one layer at the thinnest point.

The transmission curves of different film samples were measured by an ultraviolet-visible-near infrared (UV-VIS-NIR) spectrophotometer (HITACHI U-4100), and the transmission peak of broadband samples covering 490–700 nm was prepared according to this. Figure 4(e) shows the normalized transmission curve (solid green line) of the broadband sample film and compares it with the samples of each frequency band. In the figure, the transmission peaks of the eight single-frequency transmission curves are, respectively, 490 nm, 500 nm, 540 nm, 570 nm, 600 nm, 640 nm, 680 nm, and 700 nm. The transmission peak of the combined broadband sample can cover 490–700 nm (width up to 210 nm), almost including the visible spectrum. The broadband sample is proportionally equipped with the above eight single-frequency samples, and in the film and wedge sample preparation process, the various particles at the microscopic scale are automatically disordered assembly. However, experimental results show that the transmission curve of broadband thin film samples shows automatic frequency selection. Using the prism method [11,31], we then measured the refractive index of a broadband wedge sample in the range of 450–760 nm with a step length of ~10 nm [Fig. 4(f)] and compared it with the previously measured refractive index of green and red samples (green and red dotted lines). In the experimental data, the negative refractive index is observed in the incident band of 490–730 nm (bandwidth 240 nm), and the lowest value is –0.41, which is consistent with the lowest value of the negative refractive index of the red sample, but the working bandwidth is greatly increased. As can be seen, the simulation and the experiment obtained similar results, which can be confirmed by each other. The deviation comes from the inevitable discrepancy between the prepared sample and the simulated structure, but the behavior and weak interaction characteristics of the broadband samples are very well established. The resonance behavior in the theoretical curve of the broadband model is only active for the particular meta-cluster, while the other meta-clusters are not active and exhibit weak interaction properties, which are verified by the experimentally measured negative refractive index curves. The FOM measurement value of the broadband sample [$\mathrm{FOM}'_{\mathrm{exp}} = -\mathrm{Re}(n_{\mathrm{exp}})/\mathrm{Im}(n)_{\mathrm{sim}}$, for $n_{\mathrm{exp}} < 0$] fluctuated around 8 in the range of 510–700 nm, with the lowest value being 6.7 at 538 nm and the highest value reaching 13 at 592 nm [Fig. 4(g)]. It shows omnidirectional ultralow-loss characteristics in wide band. In our experiments, no less than five samples were prepared and measured at each frequency, and the measurements are very close to each other [Fig. 4(f)]. The broadband sample self-assembled by single-frequency meta-clusters can produce abnormal responses to incident light of different frequencies, which exhibits an automatic frequency

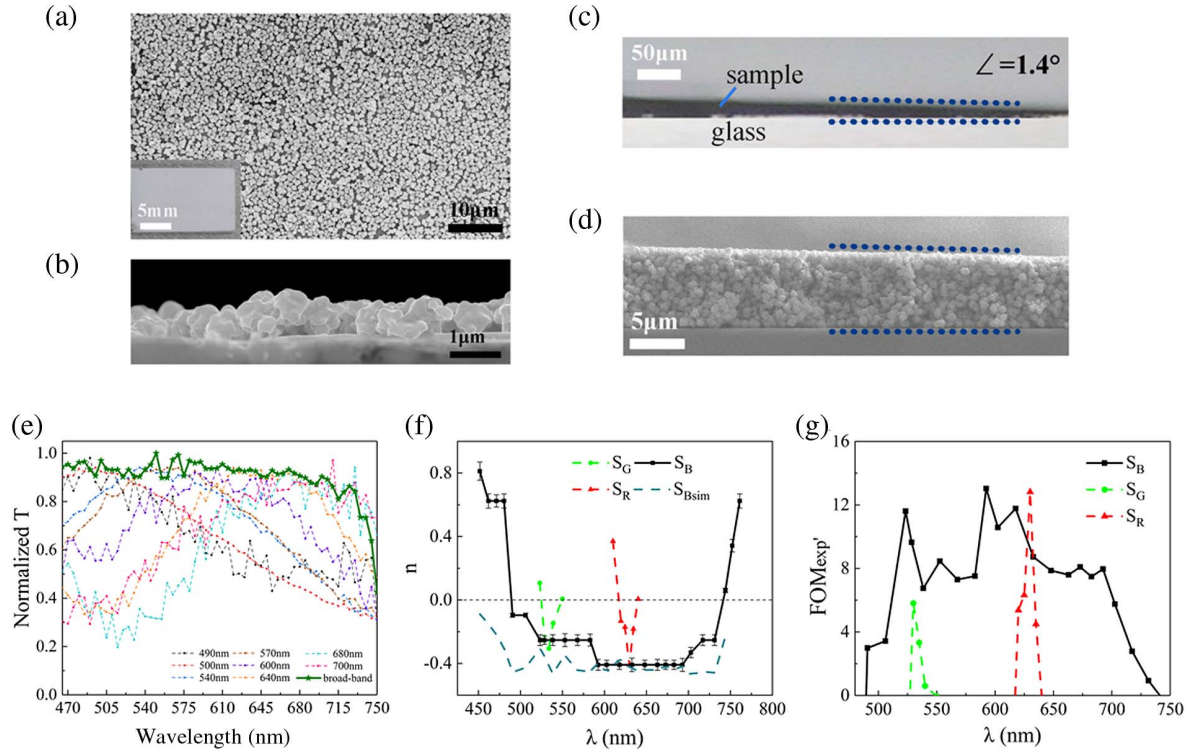

Fig. 4. Characterization of plane and 3D wedge-shaped broadband samples. (a) Plane SEM image and photograph image (the inset) of the broadband thin film sample and (b) corresponding side SEM image. (c) Microscope image of 3D wedge-shaped broadband sample and (d) corresponding SEM image, wedge angle ∼1.4°. (e) Normalized transmittance curves of broadband film sample (green line) and eight single-frequency samples (dotted line). (f) Refractive index curve measured for broadband sample S_B. The cyan dashed line is the simulated value of the broadband model from Fig. 2(o). (g) Experimental FOM values of sample S_B. Green and red curves in (f) and (g) are measured for green sample S_G and red sample S_R [31], respectively.

selection response, demonstrating the inherent feasibility and reproducibility of disordered self-assembled broadband metamaterials. The difference in refractive index of the broadband sample to different frequencies of incident light can lead to spatial spectral separation, exhibiting spatial regulation properties, as shown in Fig. 1(a). Experiments show that the meta-cluster system based on the weak interaction [35–37] assembly only needs to determine its components, but does not need to be accurate to the arrangement of each particle. The characteristics of weak interaction system metamaterials and strong interaction system PhCs are completely different, which is the embodiment of local resonance characteristics.

The fishing net structure loss of visible light metamaterials is relatively large, and the negative refraction of materials is derived indirectly and backward by simulation through measured transmission and reflection, and only the results of narrow frequency and specific orientation can be obtained [16]. Although the improved fishing net structure can broaden the frequency, only the infrared wavelength and specific incident direction can be obtained [17]. Our ultralow-loss isotropic cluster not only can be adjusted according to the need to obtain a very wide frequency, but also is not limited by the incident light direction, to achieve omnidirectional broadband.

C. Broadband Inverse Doppler Effect

The inverse Doppler effect is a fundamental property of metamaterials. Seddon and Bearpark first studied the anomalous Doppler effect in microwave gigahertz unidirectional incidence [3]. Chen *et al.* [4] designed a wedge-shaped PhC arranged by silicon rods, and measured the negative refractive index in the infrared band range; the inverse Doppler effect was observed experimentally for the first time in the infrared band (10.6 μm) along the perpendicular incidence direction. A recent study [5] has reported predicting and demonstrating the inverse Doppler effect in a specific new scene of a Vavilov–Cherenkov cone in a uniform system with a positive refractive index. Using ultralow-loss isotropic ball-thorn-shaped meta-cluster metamaterials, we observed inverse Doppler effects at red and green wavelengths for the first time, to the best of our knowledge [31]. However, the inverse Doppler effect of broadband omnidirectional visible light is still an unsolved problem.

Using the prepared broadband omnidirectional ultralow-loss sample, we measured the broadband wedge sample by refracted laser Doppler heterodyne interferometry [4,31]. The Doppler frequency shift in a sample is measured by collecting a double beam beat signal [Figs. 5(a)–5(c)]. The experiment set the motion process of the light source and the detector away from each other, and measured the Doppler frequency shift of the light source at 473 nm, 532 nm, 589 nm, 632.8 nm, and 671 nm through the sample. Figures 5(d) and 5(e) show the Doppler frequency shift curves of broadband samples measured at 532 nm, 589 nm, 632.8 nm, and 671 nm (apex angle $\theta = 1.55°$; refractive index −0.25, −0.35, −0.41, and −0.41,

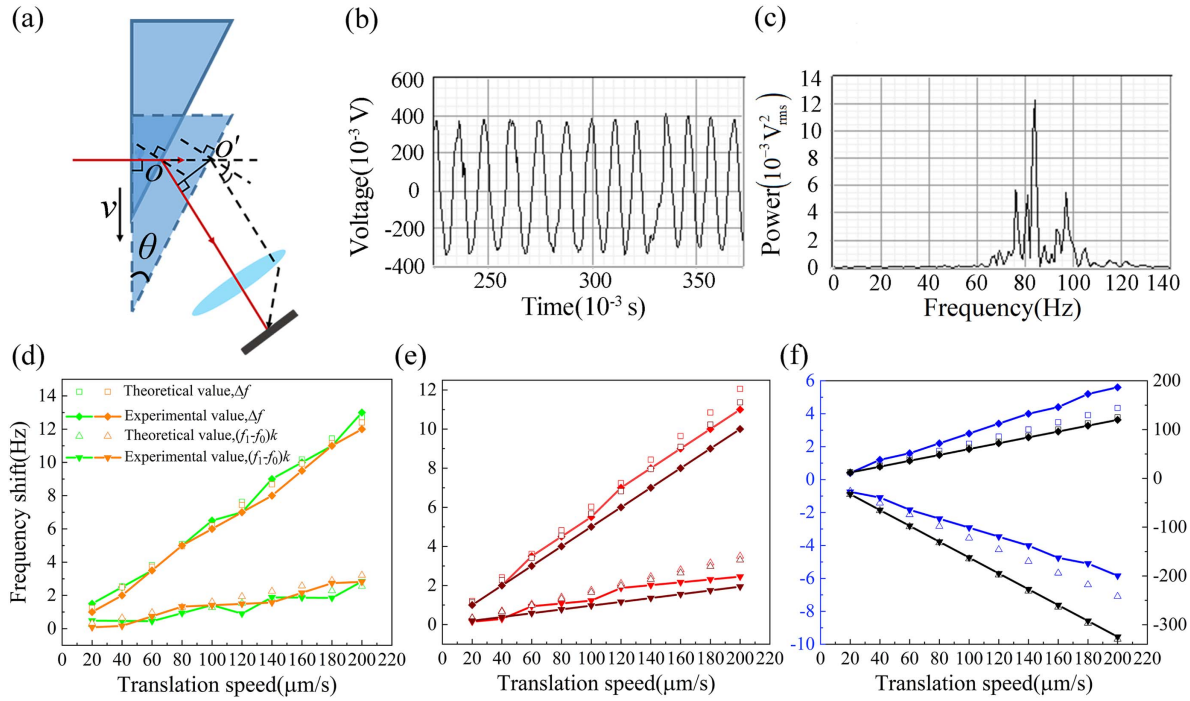

Fig. 5. Doppler effect measurement. (a) Schematic of the reference optical path when the sample moves. The size of wedge-shaped sample is 5 mm × 2 mm, wedge angle $\theta = 1.55°$, hence the allowed distance of movement is 2 mm for the laser beam. (b) and (c) Waveform map and power spectrum density map of the beat frequency signal obtained at $v = 140$ μm/s. The theoretical and measured values of beat frequency Δf and inverse Doppler frequency shift $(f_1 - f_0)k$ for broadband sample. (d) at 532 nm (green dots and curves) and 589 nm (yellow dots and curves), (e) at 632.8 nm (red dots and curves) and 671 nm (brown dots and curves); and (f) the theoretical and measured values of beat frequency Δf and Doppler frequency shift $(f_1 - f_0)k$ for broadband sample at 473 nm (blue dots and curves) and for K9 crystal [31] at 532 nm (black dots and curves).

respectively). Δf is the directly measured double beam beat frequency, f_0 is the initial frequency of the laser, f_1 is the frequency after passing through the sample, and k is infinitely close to 1. Therefore, $(f_1 - f_0)k$ represents the Doppler frequency shift occurring in the sample (see Appendix D). In the motion process of the light source and the detector away from each other, the Doppler frequency shift measured in the sample at four wavelengths is all positive (blue shift); that is, an inverse Doppler effect is observed. On the contrary, the frequency shift measured in the sample at 473 nm is red shift, which is a normal Doppler frequency shift [Fig. 5(f)]. This is very consistent with the refractive index behavior measured in Fig. 4(f) (negative refractive index range is 490–730 nm). At the speed of 200 μm/s, the maximum Doppler shift was 2.83 Hz at 532 nm, and 2.82 Hz, 2.45 Hz, and 1.94 Hz at 589 nm, 632.8 nm, and 671 nm, respectively. The results are consistent with the law of high-frequency light producing a larger Doppler shift. It should be pointed out that the inverse Doppler effect occurs in the negative refraction frequency band of the broadband sample, while the normal Doppler effect occurs in the positive refraction frequency band; even at 473 nm, $0 < n < 1$, the normal Doppler effect is still shown, which is also consistent with the principle of physics. In addition, in the assembled sample, the particles of various wavelengths are randomly distributed, but they still show an automatic frequency selection response to the abnormal behavior of the applied light wave, which provides a great convenience for the assembly of micro and nano particles. As long as the appropriate content of particles is taken into account, too much attention should not be paid to their geometric placeholder, which also reflects the completely different characteristics of the local resonance system from PhCs, phonon crystal, and other periodic structure systems.

3. DISCUSSION

This work solves the long-standing problems of narrowband, high loss, and orientation inherent in metamaterials in the visible wavelength region. Theoretical and experimental evidence demonstrates that the broadband metamaterials self-assembled by disordered meta-cluster particles at different scales can operate efficiently over a wide frequency range of omnidirectionally incident visible light and exhibit an automatic frequency selection response. It shows progress as follows.

(i) Breaking through the inherent defects of structural units. A method for assembling broadband omnidirectional ultralow-loss metamaterials is proposed, based on the conclusions of weak interactions previously found in microwave [37] and acoustic [38] regimes. The automatic frequency selection property exhibited by weak interaction provides the physical basis for the bottom-up assembly of meta-clusters; the cluster elements with different geometric sizes were developed to assemble planar films and wedge-shaped samples automatically without selection. For the first time, to the best of our knowledge, the negative refractive index in the 490–730 nm band

and broadband inverse Doppler effect were observed by using the 3D large area sample.

(ii) Solving the broadband omnidirectional problem. 3D visible spectral metamaterials are currently difficult to prepare due to limitations in size and fabrication processes; these factors significantly limit the development and possible applications of metamaterials. For example, the promising metamaterial-based optical cloaks progress slowly due to the high loss, narrowband, and orientation of the materials. Our method breaks through the difficulties of broadband and orientation in the field of metamaterials, opening the door to the preparation of 3D broadband omnidirectional visible spectral ultralow-loss metamaterials, and paving the way for the wide application of optical frequency metamaterials.

(iii) Providing a universal approach. The infrared band is a major operating spectrum in communications [39,40], and research in the terahertz band has developed rapidly in recent years [41,42]; however, both infrared and terahertz metamaterials also encounter the same challenges from high losses, narrowband, and 3D preparation. Our approach provides the basis for solving these problems and can be easily extended to these fields.

4. CONCLUSION

In summary, based on the visible spectrum broadband omnidirectional ultralow-loss meta-cluster system, we find that the abnormal behavior of the cluster disordered assembly system has the phenomenon of automatic frequency selection response and spatial regulation. The optical broadband omnidirectional metamaterials were disorderly assembled in a bottom-up method; negative refractive index and inverse Doppler effect were observed in broadband for the first time, to the best of our knowledge. The automatic frequency selection response and spatial periodic regulation of the anomalous behavior of the cluster disordered assembly system reflect the completely different characteristics between the local resonant weak interaction system of metamaterials and the strong interaction system such as PhC, and break through the physical limitations of the design of metamaterials in the visible light band. The automatic frequency selection of abnormal behavior opens the door to the down-up fabrication of 3D bulk materials and meta-fluid. This method is not only suitable for visible light, but is also easily extended to infrared and terahertz bands, paving the way for the rapid development of optical metamaterials applications.

APPENDIX A: PREPARATION OF Ag/AgCl/TiO_2@PMMA META-CLUSTER PARTICLES RESONATING IN DIFFERENT BANDS OF VISIBLE LIGHT

In Ref. [31], Ag/AgCl/TiO_2@PMMA meta-cluster particles corresponding to red-light and green-light have been prepared using the solvothermal synthesis method. Subsequently, we prepared meta-cluster particles that resonate in different bands of visible light by fine-tuning the experimental conditions. The concentration of silver nitrate solution in the whole experimental system is 0.026 g/mL: with the increase of the dosage of $TiCl_4$ (in the range of 1.0 mL to 2.2 mL), the response wavelength of the prepared particles is red shifted. A variety of meta-cluster particles with response bands ranging from blue- to red-light spectra (450–680 nm) are prepared, covering most regions of the visible light band. The concentration of silver nitrate solution in the whole experimental system is 0.0395 g/mL: various meta-cluster particles with response bands ranging from 600 nm to 700 nm are prepared by adjusting the dosage of $TiCl_4$ (1.6 mL to 2.5 mL).

APPENDIX B: PREPARATION OF Ag/AgCl/TiO_2@PMMA META-CLUSTER PARTICLES RESONATING IN VISIBLE LIGHT BROADBAND

Inspired by polychromatic light, meta-cluster mixed particles that resonate in visible light broadband (480–700 nm) are prepared.

First, we prepare meta-cluster particles resonating at the wavelength of 480–600 nm. A single-frequency meta-cluster particle is dispersed in deionized water, and the volume ratio of the sample to deionized water is about 1:5. Then, 10 μL of the samples with transmission peaks of 540 nm, 570 nm, and 600 nm are taken, respectively, for full mixing, and the transmission peak is obtained at 500–600 nm. Finally, 10 μL of the sample corresponding to 490 nm and 20 μL of the sample corresponding to 500 nm are added into the above sample to fine tune the transmission spectrum. Thus, the broadband sample with a transmission peak of 480–600 nm is obtained.

Second, we prepare meta-cluster particles resonating at the wavelength of 600–700 nm. The preparation method is similar to that described above. 10 μL of the samples with transmission peaks of 600 nm, 640 nm, 680 nm, and 700 nm are taken, respectively, for full mixing, and the broadband sample with a transmission peak of 600–700 nm is obtained.

Finally, we prepare meta-cluster particles resonating at the wavelength of 480–700 nm. The prepared samples that resonate at the wavelength of 480–600 nm and 600–700 nm are mixed in equal proportions. Then, broadband meta-clusters with transmission peak of 480–700 nm are obtained, by adding 10 μL of the sample corresponding to 700 nm into the above mixed samples for fine tuning.

APPENDIX C: PREPARATION OF PLANAR AND 3D WEDGE-SHAPED SAMPLES

Preparation of planar samples: First, a petri dish with a diameter of 10 cm is prepared and filled with deionized water (the liquid level is flush with the mouth of the glass). The prepared Ag/AgCl/TiO_2@PMMA particles are dispersed in deionized water to obtain a suspension (the volume ratio of particles to deionized water is about 1:5). Then, anhydrous ethanol is added to the suspension in a volume ratio of 1:3, followed by ultrasonic treatment of the suspension for 5 min to make the metamaterial particles evenly dispersed. The ultrasound-treated suspension is slowly injected onto the surface of ultrapure water using a syringe needle. The gradient of surface tension created by the ultrapure water causes the metamaterial particles to spread out rapidly on the water surface to form a complete monolayer film. The film is then transferred to a glass substrate

(10 mm × 50 mm). After being naturally air-dried, a uniform planar sample on the glass strip is obtained.

Preparation of 3D wedge-shaped samples: A gravity self-assembly device is set as a platform to prepare the wedge-shaped sample. The lifting slab of the experiment platform is adjusted to be horizontal. The 5 mm × 10 mm glass strip is horizontally positioned in the glass substrate, whereas another hydrophilically treated glass strip (20 mm × 40 mm) is vertically placed on the glass strip (5 mm × 10 mm) and pressed down with a proper force to ensure that the suspension will not leak during the painting. Nearly 3.5 μL of the suspension is collected using a pipette and evenly painted from one end to the other along the corner between the two orthogonal glass strips. Under the action of hydrophilicity and gravity, a wedge-shaped suspension is formed. After the water in the wedge-shaped suspension evaporates at room temperature, the horizontal glass strip containing the wedge-shaped sample with Ag/AgCl/TiO_2@PMMA particles is taken down.

APPENDIX D: MEASUREMENT OF THE DOPPLER EFFECT

The Doppler effect is measured by a high-precision laser heterodyne detection system [4,31] based on the refraction of a visible laser beam through the prepared metamaterial wedge-shaped sample. In the process of moving away from each other, the beat frequency value Δf generated by the measurement beam and the reference beam is measured directly, and the Doppler frequency shift value $(f_1 - f_0)k$ in the sample can be obtained by using the measured beat frequency Δf:

$$\Delta f = |f_2 - f_0| = |(f_1 - f_0)k + (k-1)f_0|, \quad \textbf{(D1)}$$

where f_0 is the original frequency of the laser, f_1 is the frequency of light passing through the sample at the exit position, f_2 is the frequency of light reaching the detector, $f_1 - f_0$ is the Doppler shift that occurs in the sample, and k is always positive and approaches 1 in a nonrelativistic ($v \ll c$) system. If the Doppler shift $\Delta f_D = f_1 - f_0$ in the sample is negative (that is, $f_1 < f_0$), the frequency of the light becomes smaller when the measurement beam exits from the sample during the process of being away, and the red shift phenomenon occurs; the normal Doppler effect occurs inside the sample, indicating that the sample is a normal material. Conversely, if $\Delta f_D = f_1 - f_0$ is positive (that is, $f_1 > f_0$), the blue shift phenomenon occurs during the process of being away; the inverse Doppler effect occurs inside the sample, indicating that the sample is a metamaterial.

APPENDIX E: NUMERICAL SIMULATIONS

The boundary conditions of the model are set as perfect electric conductor (PEC) in the x direction, perfect magnetic conductor (PMC) in the y direction, and open in the z direction, which is also the direction of the incident light beam. This meta-cluster unit cell model is then solved using the time domain solver in CST Microwave Studio. Based on Mie theory, the effective parameters are retrieved from the simulation results.

Funding. National Natural Science Foundation of China (52272306, 11674267).

Disclosures. The authors declare no conflicts of interest.

Data Availability. Data underlying the results presented in this paper are not publicly available at this time but may be obtained from the authors upon reasonable request.

REFERENCES

1. J. B. Pendry, D. Schurig, and D. R. Smith, "Controlling electromagnetic fields," Science **312**, 1780–1782 (2006).
2. R. A. Shelby, D. R. Smith, and S. Schultz, "Experimental verification of a negative index of refraction," Science **292**, 77–79 (2001).
3. N. Seddon and T. Bearpark, "Observation of the inverse Doppler effect," Science **302**, 1537–1540 (2003).
4. J. B. Chen, Y. Wang, B. H. Jia, T. Geng, X. P. Li, L. Feng, W. Qian, B. M. Liang, X. X. Zhang, M. Gu, and S. L. Zhuang, "Observation of the inverse Doppler effect in negative-index materials at optical frequencies," Nat. Photonics **5**, 239–242 (2011).
5. X. H. Shi, X. Lin, I. Kaminer, F. Gao, Z. J. Yang, J. D. Joannopoulos, M. Soljacic, and B. L. Zhang, "Superlight inverse Doppler effect," Nat. Phys. **14**, 1001–1005 (2018).
6. T. Ergin, N. Stenger, P. Brenner, J. B. Pendry, and M. Wegener, "Three-dimensional invisibility cloak at optical wavelengths," Science **328**, 337–339 (2010).
7. X. J. Ni, Z. J. Wong, M. Mrejen, Y. Wang, and X. Zhang, "An ultrathin invisibility skin cloak for visible light," Science **349**, 1310–1314 (2015).
8. J. B. Pendry, A. J. Holden, W. J. Stewart, and I. Youngs, "Extremely low frequency plasmons in metallic mesostructures," Phys. Rev. Lett. **76**, 4773–4776 (1996).
9. J. B. Pendry, A. J. Holden, D. J. Robbins, and W. J. Stewart, "Magnetism from conductors and enhanced nonlinear phenomena," IEEE Trans. Microw. Theory Tech. **47**, 2075–2084 (1999).
10. G. Dolling, M. Wegener, C. M. Soukoulis, and S. Linden, "Negative-index metamaterial at 780 nm wavelength," Opt. Lett. **32**, 53–55 (2007).
11. J. Valentine, S. Zhang, T. Zentgraf, E. Ulin-Avila, D. A. Genov, G. Bartal, and X. Zhang, "Three-dimensional optical metamaterial with a negative refractive index," Nature **455**, 376–379 (2008).
12. V. M. Shalaev, "Optical negative-index metamaterials," Nat. Photonics **1**, 41–48 (2007).
13. J. K. Gansel, M. Thiel, M. S. Rill, M. Decker, K. Bade, V. Saile, G. von Freymann, S. Linden, and M. Wegener, "Gold helix photonic metamaterial as broadband circular polarizer," Science **325**, 1513–1515 (2009).
14. C. M. Soukoulis and M. Wegener, "Past achievements and future challenges in the development of three-dimensional photonic metamaterials," Nat. Photonics **5**, 523–530 (2011).
15. E. Lier, D. H. Werner, C. P. Scarborough, Q. Wu, and J. A. Bossard, "An octave-bandwidth negligible-loss radiofrequency metamaterial," Nat. Mater. **10**, 216–222 (2011).
16. J. F. Wang, S. B. Qu, Z. Xu, Z. T. Fu, H. Ma, and Y. M. Yang, "A broadband three-dimensional isotropic left-handed metamaterial," J. Phys. D **42**, 155413 (2009).
17. F. Ling, Z. Q. Zhong, R. S. Huang, and B. Zhang, "A broadband tunable terahertz negative refractive index metamaterial," Sci. Rep. **8**, 9843 (2018).
18. N. Berkovitch, P. Ginzburg, and M. Orenstein, "Concave plasmonic particles: broad-band geometrical tunability in the near-infrared," Nano Lett. **10**, 1405–1408 (2010).
19. A. C. Atre, A. Garcia-Etxarri, H. Alaeian, and J. A. Dionne, "A broadband negative index metamaterial at optical frequencies," Adv. Opt. Mater. **1**, 327–333 (2013).
20. S. Bang, S. So, and J. Rho, "Realization of broadband negative refraction in visible range using vertically stacked hyperbolic metamaterials," Sci. Rep. **9**, 14093 (2019).

21. J. J. Rong and W. J. Ye, "Topology optimization design scheme for broadband non-resonant hyperbolic elastic metamaterials," Comput. Methods Appl. Math. **344**, 819–836 (2019).
22. H. C. Chu, Z. G. Chen, Y. Lai, and G. C. Ma, "Wave steering by relaying interface states in a valley-hall-derived photonic superlattice," Phys. Rev. Appl. **16**, 044006 (2021).
23. Y. C. Liu, G. P. Wang, J. B. Pendry, and S. Zhang, "All-angle reflectionless negative refraction with ideal photonic Weyl metamaterials," Light Sci. Appl. **11**, 276 (2022).
24. J. H. Huh, K. Kim, E. Im, J. Lee, Y. Cho, and S. Lee, "Exploiting colloidal metamaterials for achieving unnatural optical refractions," Adv. Mater. **32**, 2001806 (2020).
25. M. Kolle and S. Lee, "Progress and opportunities in soft photonics and biologically inspired optics," Adv. Mater. **30**, 1702669 (2018).
26. Y. Wang, J. Y. Yu, Y. F. Mao, J. Chen, S. Wang, H. Z. Chen, Y. Zhang, S. Y. Wang, X. J. Chen, T. Li, L. Zhou, R. M. Ma, S. N. Zhu, W. S. Cai, and J. Zhu, "Stable, high-performance sodium-based plasmonic devices in the near infrared," Nature **581**, 401–405 (2020).
27. V. F. Chernow, R. C. Ng, S. Y. Peng, H. A. Atwater, and J. R. Greer, "Dispersion mapping in 3-dimensional core-shell photonic crystal lattices capable of negative refraction in the mid-infrared," Nano Lett. **21**, 9102–9107 (2021).
28. I. Shutsko, M. Buchmuller, M. Meudt, and P. Gorrn, "Light-controlled fabrication of disordered hyperuniform metasurfaces," Adv. Mater. Technol. **7**, 2200086 (2022).
29. S. Yu, C. W. Qiu, Y. D. Chong, S. Torquato, and N. Park, "Engineered disorder in photonics," Nat. Rev. Mater. **6**, 226–243 (2021).
30. M. F. Xu, Q. He, M. B. Pu, F. Zhang, L. Li, D. Sang, Y. H. Guo, R. Y. Zhang, X. Li, X. L. Ma, and X. G. Luo, "Emerging long-range order from a freeform disordered metasurface," Adv. Mater. **34**, 2108709 (2022).
31. J. Zhao, H. Chen, K. Song, L. Q. Xiang, Q. Zhao, C. H. Shang, X. N. Wang, Z. J. Shen, X. F. Wu, Y. J. Hu, and X. P. Zhao, "Ultralow loss visible light metamaterials assembled by metaclusters," Nanophotonics **11**, 2953–2966 (2022).
32. B. Q. Liu, X. P. Zhao, W. R. Zhu, W. Luo, and X. C. Cheng, "Multiple pass-band optical left-handed metamaterials based on random dendritic cells," Adv. Funct. Mater. **18**, 3523–3528 (2008).
33. X. P. Zhao, "Bottom-up fabrication methods of optical metamaterials," J. Mater. Chem. **22**, 9439–9449 (2012).
34. G. A. Vinnacombe-Willson, Y. Conti, S. J. Jonas, P. S. Weiss, A. Mihi, and L. Scarabelli, "Surface lattice plasmon resonances by direct *in situ* substrate growth of gold nanoparticles in ordered arrays," Adv. Mater. **34**, 2205330 (2022).
35. X. P. Zhao, Q. Zhao, L. Kang, J. Song, and Q. H. Fu, "Defect effect of split ring resonators in left-handed metamaterials," Phys. Lett. A **346**, 87–91 (2005).
36. M. V. Gorkunov, S. A. Gredeskul, I. V. Shadrivov, and Y. S. Kivshar, "Effect of microscopic disorder on magnetic properties of metamaterials," Phys. Rev. E **73**, 056605 (2006).
37. X. P. Zhao and K. Song, "Review article: the weak interactive characteristic of resonance cells and broadband effect of metamaterials," AIP Adv. **4**, 100701 (2014).
38. S. L. Zhai, X. P. Zhao, S. Liu, F. L. Shen, L. L. Li, and C. R. Luo, "Inverse doppler effects in broadband acoustic metamaterials," Sci. Rep. **6**, 32388 (2016).
39. H. R. Barnard and G. R. Nash, "Tailoring the spectral properties of layered chiral mid-infrared metamaterials," Appl. Phys. Lett. **119**, 241102 (2021).
40. H. Zhou, D. X. Li, X. D. Hui, and X. J. Mu, "Infrared metamaterial for surface-enhanced infrared absorption spectroscopy: pushing the frontier of ultrasensitive on-chip sensing," Int. J. Optomechatron. **15**, 97–119 (2021).
41. Q. H. Wang, B. T. Gao, M. Raglione, H. X. Wang, B. J. Li, F. Toor, M. A. Arnold, and H. T. Ding, "Design, fabrication, and modulation of THz bandpass metamaterials," Laser Photon. Rev. **13**, 1900071 (2019).
42. S. Lee, S. Baek, T. T. Kim, H. Cho, S. Lee, J. H. Kang, and B. Min, "Metamaterials for enhanced optical responses and their application to active control of terahertz waves," Adv. Mater. **32**, 2000250 (2020).